NANO · MICRO small
www.small-journal.com

A Facile Strategy to Construct Silver-Modified, ZnO-Incorporated and Carbon-Coated Silicon/Porous-Carbon Nanofibers with Enhanced Lithium Storage

Jiaxin Li, Zebiao Li, Weijian Huang, Lan Chen, Fucong Lv, Mingzhong Zou, Feng Qian, Zhigao Huang, Jian Lu,* and Yangyang Li**

For Si anode materials used for lithium ion batteries (LIBs), developing an effective solution to overcome their drawbacks of large volume change and poor electronic conductivity is highly desirable. Here, the composites of ZnO-incorporated and carbon-coated silicon/porous-carbon nanofibers (ZnO-Si@C-PCNFs) are designed and synthesized via a traditional electrospinning method. The prepared ZnO-Si@C-PCNFs can obviously overcome these two drawbacks and provide excellent LIB performance with excellent rate capability and stable long cycling life of 1000 cycles with reversible capacity of 1050 mA h g^{-1} at 800 mA g^{-1}. Meanwhile, anodes of ZnO-Si@C-PCNFs attached with Ag particles display enhanced LIB performance, maintaining an average capacity of 920 mA h g^{-1} at a large current of 1800 mA g^{-1} even for 1000 cycles with negligible capacity loss and excellent reversibility. In addition, the assembling method with important practical significance for a simple pouch full cell is designed and used to evaluate the active materials. The Ag/ZnO-Si@C-PCNFs are prelithiated and assembled in full cells using $LiNi_{0.5}Co_{0.2}Mn_{0.3}O_2$(NCM523) as cathodes, exhibiting higher energy density (230 W h kg^{-1}) of 18% than that of 195 W h kg^{-1} for commercial graphite//NCM523 full pouch cells. Importantly, the comprehensive mechanisms of enhanced electrochemical kinetics originating from ZnO-incorporation and Ag-attachment are revealed in detail.

1. Introduction

The power and energy densities of lithium ion batteries (LIBs) have been increasingly demanded by the electrical equipment including intelligent robots, portable electronics, and electric vehicles.[1–3] In this regard, numerous anode materials have been extensively developed to replace the commercial graphite with limited theoretical capacity of 372 mA h g^{-1}.[4–6] Among them, Si-based materials have received considerable attention due to their superior features in terms of natural abundance, nontoxicity, low working potential, and the highest theoretical capacity of 4200 mA h g^{-1}.[7–9] However, Si-based anodes suffer from the drawbacks of large volumetric change and poor electronic conductivity, resulting in material pulverization and electrical disconnection, and further leading to cycling capacity decay.[9–11] In the past years, great research efforts have been made to circumvent the above problems and realize the practical application.

During alloying/dealloying process, the expansion and shrinkage of Si anodes during cycling would have a bad contraction stress, making the crack and stripping of Si active materials. Meanwhile, the solid electrolyte interphase (SEI) films will form successively and become thicker caused by continuous volumetric deformation of Si anode, leading to the decomposition and loss of electrolyte, large ionic transport resistance, and finally causing the failure of Si anodes.[7–11] Three main strategies have since been adopted to solve volume change for Si anodes. The first method utilizes different nano-sized structures, including particle,[12,13] sphere,[14,15] wire,[16,17]

Dr. J. Li, Z. Li, F. Lv, Prof. J. Lu, Dr. Y. Li
Hong Kong Branch of National Precious Metals Material Engineering Research Centre
Department of Material Science and Engineering
City University of Hong Kong
Hong Kong, China
E-mail: jianlu@cityu.edu.hk; yangli@cityu.edu.hk

Dr. J. Li, W. Huang, L. Chen, Dr. M. Zou, Dr. F. Qian, Prof. Z. Huang
College of Physics and Energy
Fujian Normal University
Fujian Provincial Key Laboratory of Quantum Manipulation and New Energy Materials
Fuzhou 350117, China
E-mail: zghuang@fjnu.edu.cn

The ORCID identification number(s) for the author(s) of this article can be found under https://doi.org/10.1002/smll.201900436.

DOI: 10.1002/smll.201900436

Dr. J. Li, W. Huang, L. Chen, Dr. M. Zou, Dr. F. Qian, Prof. Z. Huang
Fujian Provincial Collaborative Innovation Center for Optoelectronic Semiconductors and Efficient Devices
Xiamen 361005, China

Z. Li, F. Lv, Prof. J. Lu, Dr. Y. Li
Center for Advanced Structural Materials
City University of Hong Kong Shenzhen Research Institute
Shenzhen, China

Z. Li, Dr. Y. Li
Department of Mechanical and Biomedical Engineering
City University of Hong Kong
83 Tat Chee Avenue, Kowloon, Hong Kong

rod,[18] and film,[19] etc. Although the reports pointed out that Si active material with a size of less than critical dimension of ≈200 nm could achieve the integrity and consistency of structure and avoid its pulverization during cycled process, the nanosized Si materials cannot impede the SEI growth and keep the stability of the electrode.[2,20,21] The other strategy is to design and provide the special reserved space via pore creating and carbon-coating to further avoid the severe pulverization of Si materials.[22–24] The stable carbon coating can also improve the stability for SEI films. In addition, binders including electrically conducting polymer,[25] stretchable conductive glue polymer,[26] and self-healable supramolecular polymer,[27] play a key role in maintaining the mechanical integrity of electrodes especially for Si-based anodes in LIB. Thus, the Si anodes with nanosized structure also combined with enough reserved space could overcome large volumetric change and obtain the improved LIB performance.

The other question encountered by the Si anode in practical implication is its poor conductivity, inevitably leading to electrode polarization and low reactivity and attenuating the LIB performance. Numerous carbon materials including carbon nanotubes,[28] graphene,[29,30] and carbon nanofibers[31,32] have been used to coat and/or support the different Si materials for forming stable Si-based anodes. However, introducing carbon nanomaterials will inevitably decrease the initial coulombic efficiency (ICE) for anodic composites.[9] Accordingly, great efforts have been devoted to releasing the irreversible capacity loss from the SEI film for anodic nanocarbon materials. It is proved that noncarbonic materials, such as ZnO,[33,34] Al_2O_3,[35] and metal (i.e., Ag, Cu, Al) nanoparticles,[36–39] can effectively improve the conductivity and maintain the integrity of Si composites and the stability of the SEI layer. Zhu's group had developed composites of ZnO coated Si nanoparticles and nanowires, showing significantly improved electrochemical performance mainly caused by enhanced mechanical integrity and stabilized interface contributed from ZnO coating.[33] Very recently, Kim et al. reported their electrodes using nanoporous ZnO to coat on a Si microparticle, which can accommodate extreme Si volume expansion, facilitate stable cycling performance and obtain large ICE.[34] Furthermore, it is reported that Ag metal particles with conducting activity can release the polarization of electrodes and remarkably boost their LIB performance for silicon based anodes.[36,37] Hence, for LIBs, reasonable design of Si-based anodes with stable structure, good conductivity, and enhanced CE is highly needed.

In fact, each of the above-discussed strategies, such as size control, morphology modulation, carbon-coating/supporting, as well as introduction of noncarbonic materials, can improve the LIB performance of Si-based anodes on a certain extent. However, the key-point is how to develop a simple method to effectively optimize the prepared conditions combined with the synergy of several strategies, and finally achieve the obtaining of high-performance Si-anode materials.

In this work, the traditional electrospinning method was designed to synthesize the anodes of Ag-modified, ZnO-incorporated, and carbon-coated silicon/porous-carbon nanofibers (marked as Ag/ZnO-Si@C-PCNFs). The ZnO-Si@C-PCNF and Ag/ZnO-Si@C-PCNF anodes can deliver excellent LIB performance due to the following advantages: a) the used Si particles were smaller than the critical expansion size and coated by the pyrolytic carbon layer from PAN, withstanding the volumetric changes of Si particles and relieving their pulverization, b) numerous inner pores in CNFs originated from vaporization of ZnO provide reserved space for Si expansion and electrolyte storage, being similar to the previous studies,[9,22] c) the trace ZnO residues could promote the stability of CE and resists the Si agglomeration, thus improving the structural stability and ionic conductivity; d) the CNF skeleton maintained stably and incorporated with Ag metal nanoparticles can effectively enhance electronic conductance, reduce polarization, and further improve the LIB performance. In addition, the mechanism of enhanced electrochemical kinetics was revealed in detail. The simple pouch full cell have been designed and presented, which is of great significance to other researchers.

2. Results and Discussion

2.1. Morphology and Structure

Scanning electron microscope (SEM) measurement was used to detect the morphology of the Si@C-PCNFs and ZnO-Si@C-PCNFs, and the results are shown in **Figure 1**a–d (also see Figure S1 in the Supporting Information). The SEM images for these two samples show that all nanofibers appear to have a similar structure with continuous and cross-linked network and agglomerates of Si nanoparticles (NPs) embedded in or attached on carbon nanofibers; that is, the adding ZnO would not change the composite's structure. The appearance of Si NPs becomes blurred due to the coating carbon layer. Herein, The silicon content of ZnO-Si@C-PCNFs is about 29.7 wt% as shown in Figure S2 in the Supporting Information.

The X-ray diffraction (XRD) results shown in **Figure 2**a reveal the crystalline phases. Both samples display obvious diffraction peaks at 28.6°, 47.4°, and 56.3°, assigned to (111), (220), and (311) reflections of Si NPs, respectively (JCPDS card no. 27-1402).[30] Little broad peaks around 26° could be assigned to reflections of carbon nanofibers. The peaks for ZnO cannot be detected in XRD pattern due to its low content and uniform distribution in ZnO-Si@C-PCNFs. After annealing at 900 °C, most ZnO evaporated and the remaining content of ZnO in sample is ≈1.6 wt% obtained from inductively coupled plasma optical emission spectroscopy (ICP) test. The insets in Figure 2b compare the Brunner–Emmet–Teller (BET) results of the Si@C-PCNFs and ZnO-Si@C-PCNFs. The values of specific surface area for Si@C-PCNFs and ZnO-Si@C-PCNFs are 45.18 and 87.89 $m^2\ g^{-1}$, respectively. Compared to Si@C-PCNFs, the ZnO-Si@C-PCNFs can provide larger specific surface area, which indicates the effect of the ZnO evaporation and its pore creating. In addition, the Barrett–Joyner–Halenda (BJH) pore size distribution shown in Figure 2b also shows that 2–3 nm pores and mesopores are in majority for ZnO-Si@C-PCNFs, more than that of Si@C-PCNFs. The relatively more pores can store electrolyte, boost the ion transport and withstand the volumetric changes of Si NPs, thus ensuring good LIB performance at high currents.[40]

As previously reported, the modification of ZnO and its loading morphology are very important for improving the

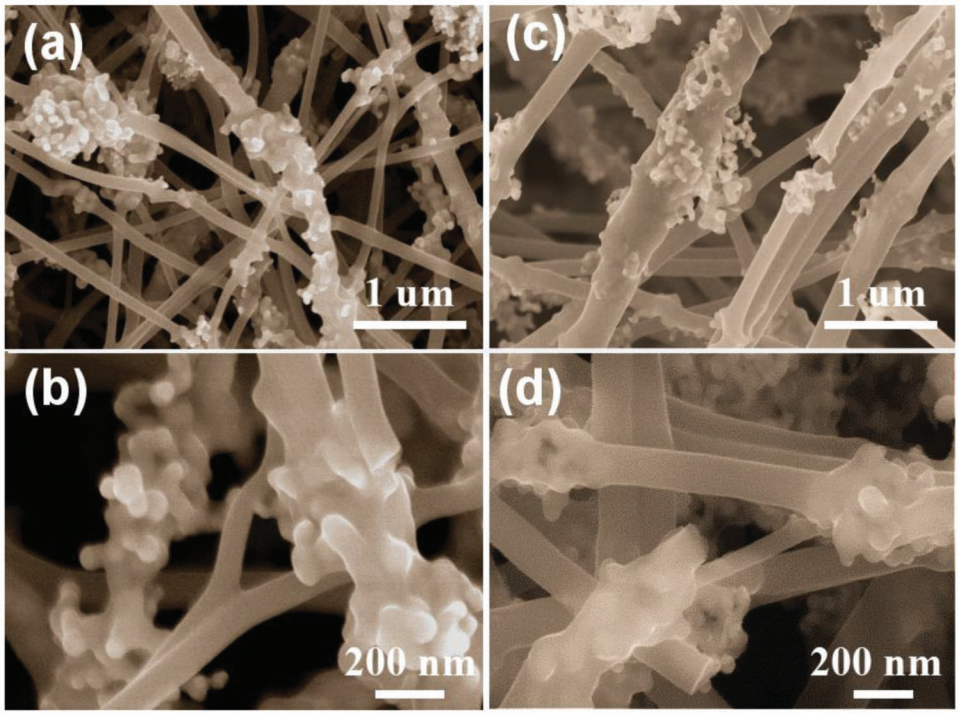

Figure 1. SEM and magnified SEM images of a,b) Si@C-PCNFs and c,d) ZnO-Si@C-PCNFs.

performance of Si-based anodes.[33,34] Along with SEM, TEM was used to examine the detailed structure of ZnO-Si@C-PCNFs. The representative TEM image in **Figure 3**a clearly displays that Si NPs coated with carbon layer and their agglomerates are embedded in or bonded to CNFs like the schematic illustration shown in **Figure 4**. The similar structure can be found for Si@C-PCNFs (see Figure S3 in the Supporting Information). Herein, the used Si NPs have an average particle size of 60 ± 15 nm as counted and presented in Figure S4 in the Supporting Information, being smaller than the critical expansion size of ≈200 nm.[20,21] As revealed in Figure 3b, high-resolution transmission electron microscopy (HR-TEM) image shows that Si lattice spacing of 0.312 nm corresponds to the (111) plane and the well-coated carbon layer is found with a thickness distribution of 8 ± 2 nm (also displayed in Figure S5 in the Supporting Information). The ratio of the size of Si radius to the thickness of carbon layer is estimated as 2.3–6.8, which value played an important role in the integrity of core–shell structure.[21] In addition, such carbon layers can help Si NPs avoid contacting with electrolyte, therefore impeding the excessive formation of SEI film. The selected area electron diffraction (SAED) measurement was also provided to investigate detailed crystal information about ZnO-Si@C-PCNFs (see Figure 3c). The corresponding diffraction rings of (111), (200), and (311) planes for Si are obviously distinguished, being consistent with the XRD result.

To find the evidence of existence for the ZnO modification, bright field (BF) TEM and dark field (DF) TEM were carried out and shown in Figure 3d,e. The same areas were selected and compared under bright and dark field test. The BF-TEM image in Figure 3d shows that Si NPs possesses spheroidal geometrical morphology. On the contrary, it can be seen from

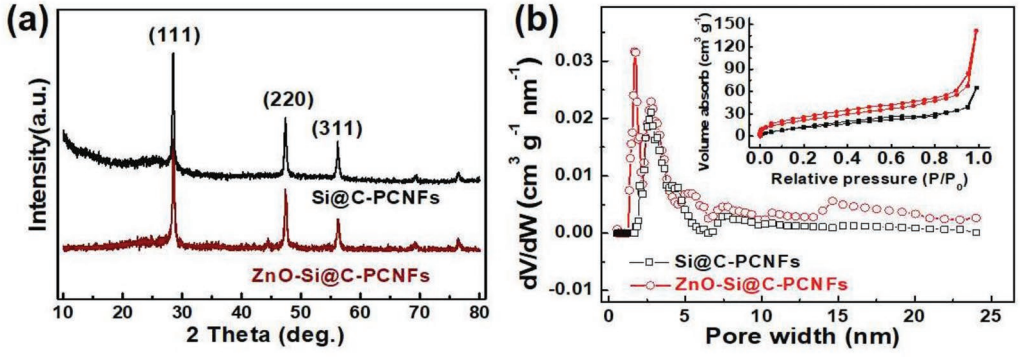

Figure 2. a) XRD pattern and b) N_2 adsorption–desorption isotherm and BJH model pore size distribution of the Si@C-PCNFs and ZnO-Si@C-PCNFs.

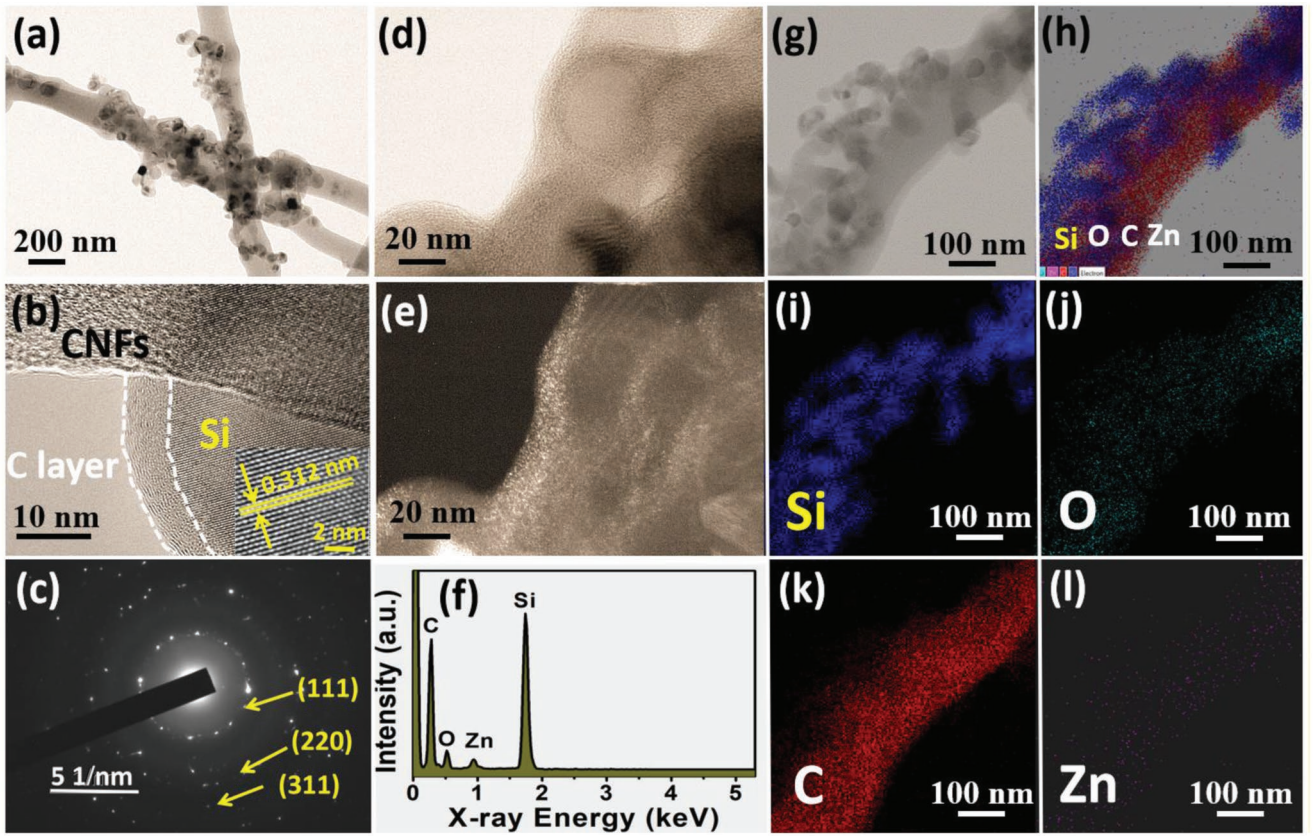

Figure 3. a) TEM image, b) HR-TEM image, c) SAED result, d) bright field (BF) TEM image, e) dark field (DF) TEM image and f) EDS result of ZnO-Si@C-PCNFs; g–l) Si, O, C, and Zn STEM/EDS elemental mapping of ZnO-Si@C-PCNFs.

the DF-TEM image in Figure 3e that some bright spots believed to be ZnO were covered by shallow grey flocculent matter of carbon layer, suggesting that atomic ZnO was uniformly embedded in carbon layer. In addition, the Zn component can be detected by energy dispersive spectroscopy (EDS) as revealed in Figure 3f. Figure 3g–l shows the STEM/EDS elemental mapping used to further check the element composition. It can be seen that C, O, Zn, and Si elements are regularly distributed in the ZnO-Si@C-PCNF composite, which means Si NPs covered by carbon layer combined with ZnO material.

2.2. Electrochemical LIB Performance

To study the intrinsic LIB performance of the anodes of Si@C-PCNFs and ZnO-Si@C-PCNFs, CR2025 coin-type half-cells with Li foil as counter electrodes were examined under different test conditions. **Figure 5**a,b displays the cyclic voltammogram (CV) curves conducted for the initial five cycles with the potential range between 0.01 and 3.0 V to investigate the redox process of the anodes for Si@C-PCNFs and ZnO-Si@C-PCNFs. For both anodes, the 1st CV curve is quite different from those subsequent four cycles. The large reductive peaks at 1.0–0.5 V and the following broad peak continued to 0.01 V presented in both anodes indicates the occurrence of the SEI film production, the formation of a Li–Si alloy, and Li ions insertion to the CNFs, respectively. Broad peaks of the two anodes observed at 0.10–0.55 V correspond to the dealloying reaction of Li_xSi, being similar to other reports.[23] The large peaks of 1.0–0.5 V in the 1st half-cycles disappear in the subsequent four cycles for both anodes caused by the irreversible transformation of the SEI film.[24] In addition to the redox peaks for ZnO-Si@C-PCNF

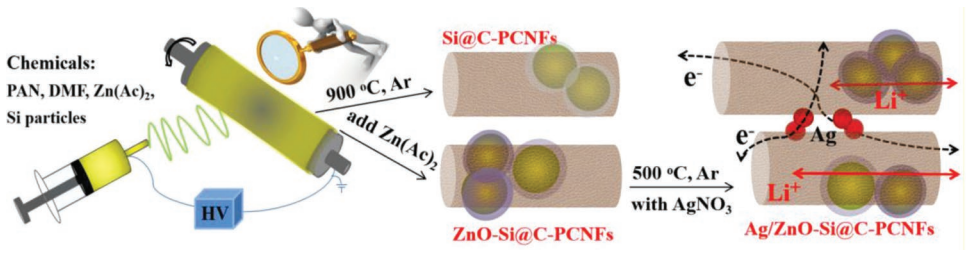

Figure 4. Schematic illustrations of the experimental procedure.

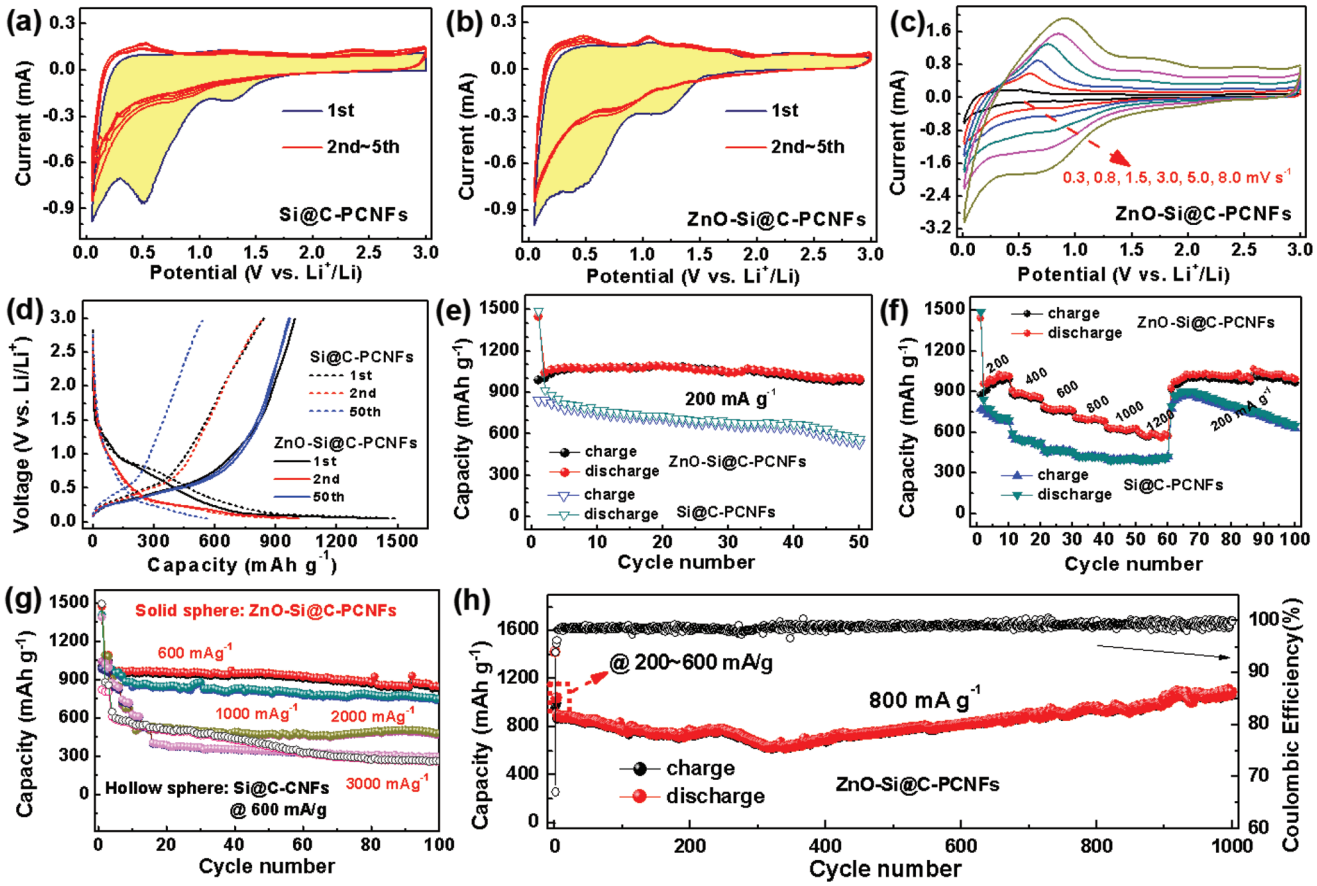

Figure 5. Electrochemical performance of the Si@C-PCNF and ZnO-Si@C-PCNF anodes for LIBs. a–c) Cyclic voltammogram (CV) curves between 0.05 and 3.0 V, d) Typical discharge–charge profiles tested at 200 mA g^{-1}, and e–h) cycling performance, rate capabilities at various and long-term cycling performance.

anode shown in Figure 5b, the large reductive peak at the 1st cycle contains the reduction of little ZnO to metallic Zn, and the formation of a Li–Zn alloy; the broad anodic peaks at 1.0–1.45 V are assigned to its dealloying reaction, together with the oxidation of Zn to Zn^{2+}.[41] The forming Li_2O/Zn derived from conversion reaction of ZnO and Li ions, as an ionically and electrically conductive matrix, can prevent extensive pulverization that contributed to the overall electrode capacity and stability.[34] The CV curves for the following four cycles overlap well, indicating good stability for LIBs. Furthermore, the CV curves of ZnO-Si@C-PCNFs at different rates deliver similar redox peak shapes as presented in Figure 5c, revealing this electrode exhibits good electrochemical response under various current rates.

Figure 5d gives the representative galvanostatic discharge/charge (D/C) profiles of Si@C-PCNF and ZnO-Si@C-PCNF electrodes. The ZnO-Si@C-PCNF sample delivers D/C reversible capacities of 1486 and 995 mA h g^{-1} with a larger initial coulombic efficiency (ICE) of 68.9%, than that of 58.0% (i.e., 1456 and 845 mA h g^{-1}) for Si@C-PCNF sample. This result reveals that the sample with ZnO modification can obtain stable SEI film caused by the reaction between ZnO and electrolyte. This result can also be supported by the SEM result for SEI film as shown in the following **Figure 6**a,c. Additionally, the charge capacities from the 2nd to 50th cycles for ZnO-Si@C-PCNFs fell at ≈970 mA h g^{-1}, with no obvious capacity loss. However, that capacity for Si@C-PCNFs only remains 549 mA h g^{-1} after 50 cycles, with a large capacity loss of 35.5%. The corresponding LIB cycling stability is compared and shown in Figure 5e. Additionally, the values of cycling CE of these two samples have been compared in Figure S6 in the Supporting Information. As expected, the ZnO-Si@C-PCNFs provide a larger CE value of 98.5–99.5% than that of 97.6–98.8% for Si@C-PCNFs after the initial activated several cycles. Thus, it is easy to conclude that the obtained large ICE, CE, and stable cycling performance for ZnO-Si@C-PCNFs can be ascribed to the additional ZnO modification to carbon layer and CNFs, which enhanced mechanism would be discussed in detail in the following Figure 6. With regard to the rate performance, these two samples were examined at various D/C current densities from 200–1200 mA h g^{-1}. It can be seen from Figure 5f that ZnO-Si@C-PCNFs exhibit gradual reduced but stable specific capacities at each rate, much better than Si@C-PCNFs. Even recovering to current of 200 mA g^{-1}, the reversible capacity is still 984 mA hg^{-1} stably cycled for 40 times, or 99% of the initial capacity at 200 mA g^{-1} for the first ten cycles, demonstrating the stable cycling performance. Correspondingly, the relative long cycling of 100 cycles for Si@C-PCNFs and ZnO-Si@C-PCNFs are also compared in Figure 5g at different rates. The reversible capacities for ZnO-Si@C-PCNFs tested at 600, 1000, 2000, and 3000 mA g^{-1} exhibit only slight attenuation.

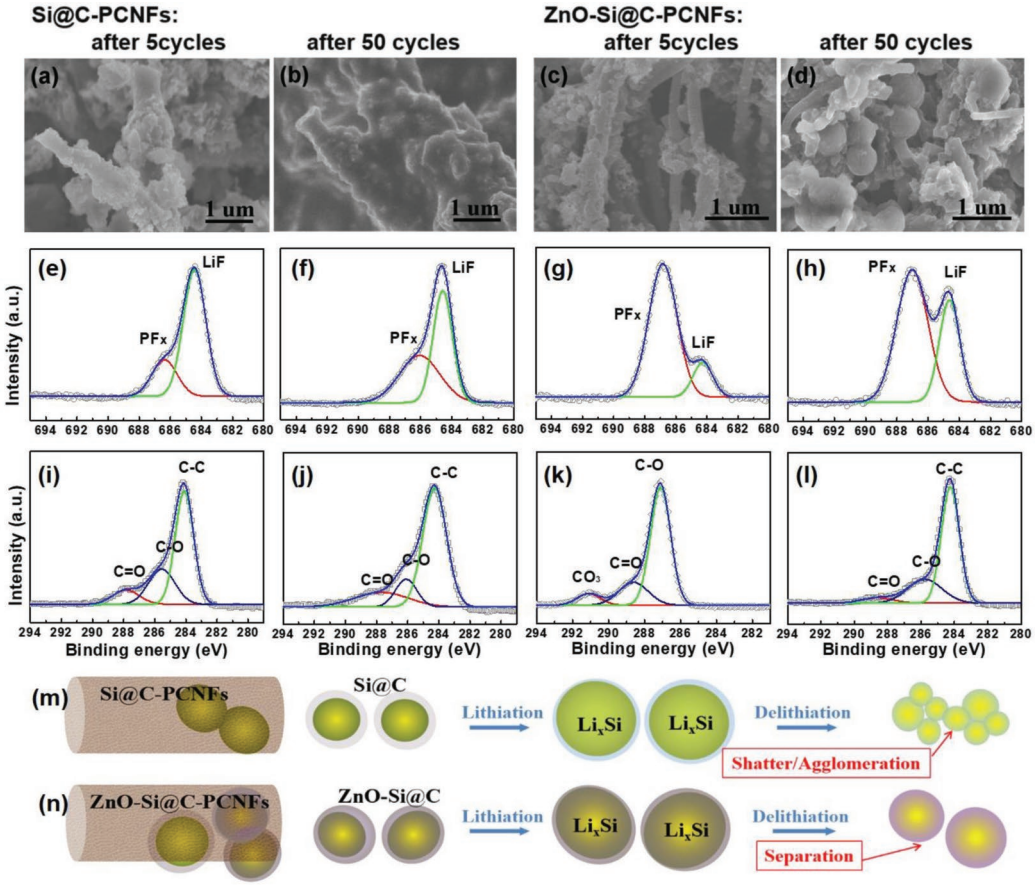

Figure 6. SEM images for Si@C-PCNFs and ZnO-Si@C-PCNFs of a,c) after 5 cycles, and b,d) after 50 cycles; the corresponding XPS spectra for Si@C-PCNFs and ZnO-Si@C-PCNFs of e,g) F 1s after 5 cycles, f,h) F 1s after 50 cycles, i,k) C 1s after 5 cycles, and j,l) C 1s after 50 cycles; m,n) schematic illustration of the Si particle agglomerated in Si@C-PCNFs and ZnO-Si@C-PCNFs with and without the ZnO additive.

However, an obvious capacity loss from 600 to 290 mA h g^{-1} appears in Si@C-PCNFs when tested at only 600 mA g^{-1}, which could be caused by serious structural failure. This phenomenon can also be indirectly proved by the electrochemical impedance spectroscopy (EIS) results for these two electrodes before and after cycling test (see discussion shown in Figure S7 in the Supporting Information). At a glance, the anode of ZnO-Si@C-PCNF also delivers a superior cycling performance with a reversible capacity of ≈1050 mA h g^{-1} for 1000 cycles at 800 mA g^{-1} as shown in Figure 5h, along with a large CE larger than 99.2%, confirming good tolerance for the fast Li ions transmission process and its potential application for long-cycling LIBs. In addition, it can be found that the little capacity fading exhibited in the first 320 cycles and an increasing trend of the capacity observed in the following cycles. In the early cycling process, the Si electrodes still suffer severe mechanical degradation due to the volume change inherently accompanying with conversion reaction. After the structure refinement and formation of a stable SEI, the reactivated electrode can exhibit an excellent reversible capacity and a good cycling stability after an extremely long cycle especially at relative high rates.[42,43] As compared in Table S1 in the Supporting Information, such LIB performance is comparable to some best results in recent reports.

2.3. Discussion for Enhanced Mechanism

The recent work reported that the ZnO coating or mixing can reduce the electrode crack and enhance their LIB performance.[33,34] Especially, although the enhanced mechanistic benefit of ZnO adding is indisputable, other comprehensive roles of the ZnO adding, especially with trace adding, are still unclear.[34] Here, SEM and X-ray photoelectron spectroscopy (XPS) analyses were carried out and used to detect the changes of the Si@C-PCNF and ZnO-Si@C-PCNF electrodes after different cycling and reveal the enhanced electrochemical mechanism of ZnO modification. Figure 6a–d respectively display the SEM images for electrodes of Si@C-PCNFs and ZnO-Si@C-PCNFs after 5 and 50 cycles tested at 200 mA g^{-1}. It can be observed from SEM image shown in Figure 6a for Si@C-PCNFs that the PCNFs skeleton maintained stably, in which the Si@C particles have been obviously crushed without their original spherical structures after 5 cycles. For Si@C-PCNFs after 50 cycles presented in Figure 6b, the diameter of PCNFs becomes coarse, most of Si@C particles are crushed and agglomerated, and the electrode has been covered with a thick film. It is inferred that the thick film should belong to the SEI film, which will reduce the effective contact between materials and electrolyte in the subsequent cycles, resulting in

poor LIB performance. However, the compared SEM image of Figure 6c for ZnO-Si@C-PCNFs shows that the Si@C particles are slightly enlarged and maintain their original spherical structures attaching on the PCNFs after 5 cycles, which result is significantly different from that of Si@C-PCNFs. Usually, the Li salt of $LiPF_6$ for the LIB electrolyte could decomposes and forms HF, which would etch the surface oxide layer of SiO_2 and form a labile Si–H thin layer, leading to the agglomeration of Si particles during the volume changes.[35] Such agglomeration of Si@C particles deteriorates the electrical contacts, resulting in unfavorable cycling LIB performance. Besides, the presence of the ZnO consumes the HF, protecting the Si@C NPs that prevents their agglomeration. Therefore, the Si@C NPs with ZnO modification can dispersed well during electrochemical test, further delivering an outstanding LIB performance. Interestingly, further compared with Si@C-PCNFs after 50 cycles, the electrode still present a loosened structure as shown in Figure 6d. The spherical Si@C particles are obviously enlarged, which should be caused by the expansion and shrinkage of Si anodes and the continuous forming of SEI layer. The maintained structure can promote electrolyte to continuously penetrate in the electrode layer, obtain stable conductive contact and thus boost the LIB performance.

The XPS spectra of the Si@C-PCNFs and ZnO-Si@C-PCNFs after 5 and 50 cycles displayed in Figure 6e–l and Figures S8 and S9 in the Supporting Information, was conducted to reveal the SEI components found in surface of tested electrodes and further shed light on the modification effect of trace ZnO modification. From the comparison of Figure 6e–h, the F 1s signal for ZnO-Si@C-PCNF electrode shows an predominant peak of organic fluorine at 688.5 eV combined with a little peak at 684.5 eV for metal fluorides after initial 5 cycles, and delivers these two peaks with similar strength after 50 cycles, indicating the main component of $LiPF_x$ for both cases after 5 and 50 cycles.[35] However, Si@C-PCNF electrodes without ZnO modification show predominantly metal fluorides after 5 and 50 cycles, illustrating that the SEI film forms at the initial cycling progresses. The decomposition progress of electrolyte can be effectively delayed with the modified ZnO, also revealing that the modification of ZnO can promote the interfacial stability of electrolyte and electrode materials. As can be seen from the C 1s peaks in Figure 6i–l, the ZnO-Si@C-PCNF electrode shows the presence of Li_2CO_3 species after 5 cycles which are known to be a stable SEI component; contrarily, organic component for SEI is formed in the initial stage without ZnO modification, which is considered to be unstable.[34] Meanwhile, the phenomenon is consistent with that of O 1s and Li 1s XPS signals observed from Figure S9 in the Supporting Information. This result reveals that ZnO modification can promote the interface stability between active materials and electrolyte, and significantly affect the growth of SEI layer and the morphology of electrodes. The current result can reveal that the sample with ZnO modification can possess a slower interface deterioration between electrolyte and Si anode. Figure 6m,n illustrate a comprehensive mechanism of the protective role of ZnO modification based on the obtained results in this work. Although the Zn 2p signal on the SEI surface has not been detected due to the limited detection capability of XPS, the following conclusions could be deduced from the above results and the related reports.[34] HF formed in batteries etches the Si surface and form labile Si—H bonds, leading to the agglomeration for Si NPs. However, when ZnO is modified on Si@C-PCNFs, the HF will react with ZnO and yield ZnF_2, avoiding the formation of Si–H surface. Thus, the ZnO-Si@C NPs can be separated effectively and the electrical contacts can be remained and the LIB performance can be further improved.

2.4. Improvement and Practical Implication

Based on the above-obtained result, it is acceptable for the ZnO-Si@C-PCNFs with 29.7% Si content delivering such LIB performance also compared in Table S1 in the Supporting Information. Moreover, the relative mechanism explanation proves that the stability strategy improved by trace ZnO modification is feasible. However, as shown in Figure 5e, taking the cycling capacity at 200 mA g^{-1} to analyze, the reversible capacity contribution from silicon material is only ≈57% of its theoretical value (see Discussion Part in Supporting Information). To further release its reversible capacity is important and indispensable. Usually, adding metal conductive particles to composites can effectively enhance their conductivity and reduce their polarization voltage, and thus release more reversible capacity from silicon active material.[36–39] Compared with ZnO-Si@C-PCNFs shown in Figure 1c,d, it can be seen from **Figure 7**a–f that attaching Ag NPs on ZnO-Si@C-PCNFs does not change their original structures. In addition, the SEM and TEM images show that the Ag NPs with 6–12 nm in size uniformly adhere to the ZnO-Si@C-PCNFs skeleton. The XRD, XPS, and elemental mapping of Ag/ZnO-Si@C-PCNFs are provided in Figures S9 to S11 in the Supporting Information. Such materials with Ag NPs attachment possess a lot of metal joints, which can significantly get good conductivity and enhance LIB performance. The EIS data shown in Figure S12 in the Supporting Information also supports this result.

Accordingly, the electrochemical properties have been displayed in Figure 7g,h. Herein, the related D/C curves for Ag/ZnO-Si@C-PCNFs are provided in Figures S13 and S14 in the Supporting Information. Fairly stable capacity of 1130 mA h g^{-1} tested at a current densities of 300 mA g^{-1} can be detected for 100 cycles as observed in Figure 7g, corresponding to ≈75% of theoretical capacity of 4200 mA h g^{-1} for silicon material (see Discussion Part in Supporting Information), being much better than that of ZnO-Si@C-PCNFs without attaching Ag NPs. The further test of long cycling performance tested at 1800 mA g^{-1} after being activated at 300, 600, and 1200 mA g^{-1} in the first 15 cycles has been also carried out and displayed in Figure 7h. The Ag/ZnO-Si@C-PCNFs can deliver an average reversible capacity of ≈920 mA h g^{-1} even after 1000 cycles. Furthermore, the CE values fall between 98.5% and 99.9%, which is slightly better than that of ZnO-Si@C-PCNFs. This obtained LIB performance revealed that adding Ag NPs combined with trace ZnO modification can obviously reduce the electrodes' interface polarization, enhance their conductivity, and finally improve their LIB performance. According to the previous reports,[44,45] metallic components including Ag may act as diffusion barrier to limit the full lithiation of silicon, and the inhibition of its phase transition greatly improves their structural stability and

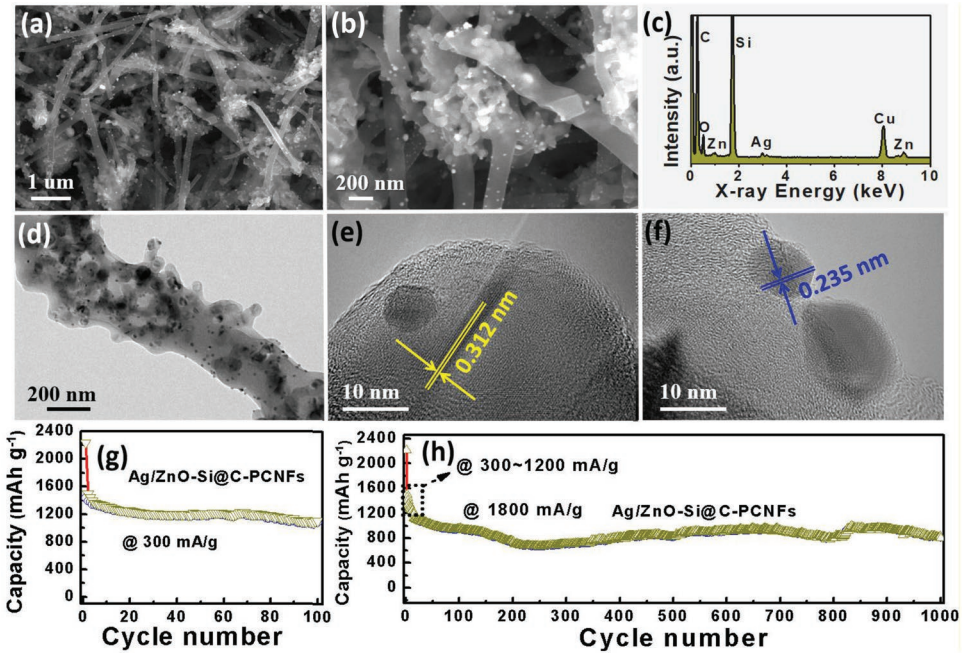

Figure 7. a) SEM image, b) magnified SEM image, c) EDS pattern, d) TEM image, and e,f) HR-TEM image of Ag/ZnO-Si@C-PCNFs. g) Cycling performance tested at 200 mA g^{-1} and h) long-term cycling performance tested at 1800 mA g^{-1} for Ag/ZnO-Si@C-PCNF electrodes.

cyclic life. In particular, a comparison between this work and the recently reported excellent Si-based anodes has been compared in Table S1 in the Supporting Information, indicating the performance for Ag/ZnO-Si@C-PCNFs is better than most similar reports on Si/C anodes.

To further evaluate the possibility of commercial application for LIBs, simple pouch full cells comprising anode of Ag/ZnO-Si@C-PCNFs and cathode of $LiNi_{0.5}Co_{0.2}Mn_{0.3}O_2$ (NCM523) have been designed and assembled (see Figure S15 in Supporting Information). The electrodes have been prepared according on commercial full battery standard. Before the full-cell test, the Ag/ZnO-Si@C-PCNF electrodes were first prelithiated via direct touch with Li foil under the presence of electrolyte, and then used as anodes for full batteries.[46,47] Subsequently, the assembled batteries need to undergo a rigorous activation process and then collect their cycling performance as shown in **Figure 8**. The Ag/ZnO-Si@C-PCNFs//NCM523 full cells were tested between 3.0 and 4.2 V. Considering that the capacity fluctuation of Ag/ZnO-Si@C-PCNFs is larger than that of commercial graphite, the electrode capacity ratio for anode/cathode is 1.20, being slightly larger than 1.08 for commercial graphite//NCM523 full cells. The specific capacity of the full cell was calculated based on the weight of NCM523 cathode. As expected, the full cells can deliver reversible capacity of ≈135 mA h g^{-1} at 0.2 C (i.e., 30 mA g^{-1}) for 50 cycles (Figure 8a) and good rate performance (Figure 8b), which values are similar to the NCM523 cathodes.[48] The insets of Figure 8a,b display the corresponding D/C curves of the full cells for different cycles at varied current densities. The cycling D/C voltage plateaus are all at around 3.70 V. Herein, anodes of Ag/ZnO-Si@C-PCNFs with mass loading of 3.1 ± 0.1 mg cm^{-2} are used to replace graphite anodes with mass loading of 10.0 mg cm^{-2} for simple pouch full cells. Measurements of the cycling performance of these full cells deliver areal capacity ≈3.0 mA h cm^{-2}, reaching that of 455565-sized commercial full cells of graphite//NCM523. Thus, the obtained full cells of Ag/ZnO-Si@C-PCNFs//NCM523 can deliver mass energy density value of 230 W h kg^{-1}, being larger ≈18% than that of 195 W h kg^{-1} for graphite//NCM523 calculated based on the full-size commercial full cell standard. The related details on calculations are presented in supporting discussion presented for Figures S16 and S17 in the Supporting Information. In addition, as shown in Figure 8c, the simple pouch full cell used as a power source can simultaneously light light two light emitting diode (LED) screens and drive motor to rotate rapidly, delivering a stable energy output. Unlike most previous reports[49–52] based on coin-sized full battery routine without considering comprehensive assessment on real factors including the weight of the electrolyte, current collector, separator, and case in a pouch cell configuration, the obtained results in this work can provide more practical reference value for LIBs. Undoubtedly, this refined method about simple pouch full cell show great potential in the application of fundamental research for other researchers and the successful Ag/ZnO-Si@C-PCNF composite has a great commercial potential for the high-performance LIBs.

3. Conclusion

In summary, the composites of ZnO-Si@C-PCNFs and Ag/ZnO-Si@C-PCNFs have been designed and easily synthesized via traditional electrospinning method. The prepared composites possessed unique nanostructure and excellent conductivity can deliver excellent LIB performance especially with stable long cycling life of 1000 cycles with reversible capacities of ≈1050 mA h g^{-1} at 800 mA g^{-1} and ≈920 mA h g^{-1} at

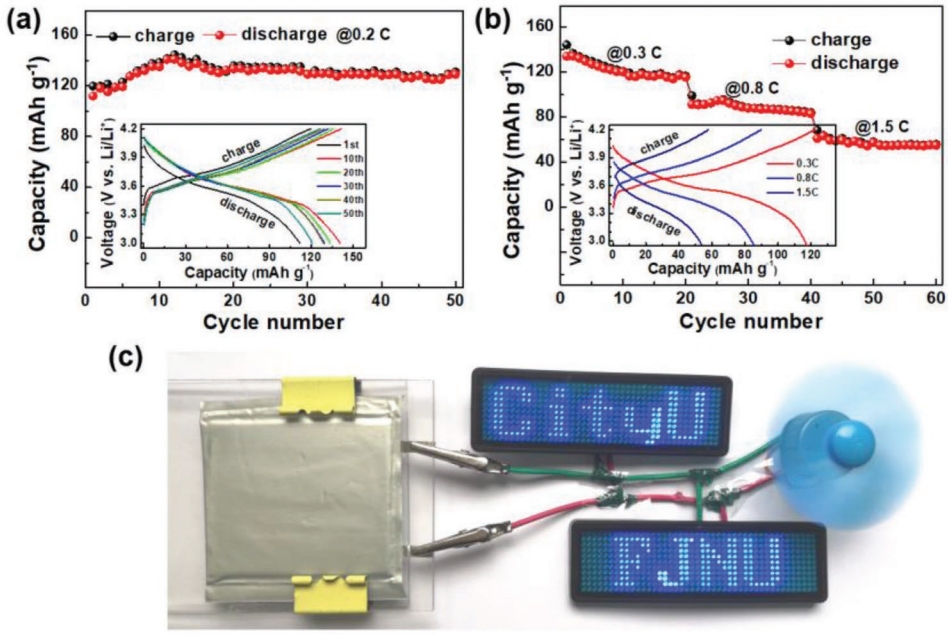

Figure 8. Electrochemical characterization of Ag/ZnO-Si@C-PCNFs//NCM523 full cells: a) cycling performance at 0.2 C, the inset shows galvanostatic charge–discharge profiles; b) rate performance; the inset shows galvanostatic charge–discharge profiles; c) the full cell can power two LED screens and motor.

relative large current of 1800 mA g^{-1}. Importantly, the comprehensive mechanisms of enhanced electrochemical kinetics originating from ZnO-incorporation and Ag-attachment have been revealed in detail. In addition, the assembling method with important practical significance for simple pouch full cell has been designed and used to evaluate these active materials. The pouch full cells with Ag/ZnO-Si@C-PCNF anodes and $LiNi_{0.5}Co_{0.2}Mn_{0.3}O_2$(NCM523) cathodes can provide energy density of 230 W h kg^{-1}, being ≈18% higher than that of commercial graphite//NCM523 full pouch cells. It is believed that the design concept for silicon anode materials and the technology for simple pouch full cell can serve as a promising reference for other researchers.

4. Experimental Section

Material Synthesis and Characterization: In this work, all chemicals were purchased and used without further purification. The samples were all prepared by an electrospinning method as shown in Figure 4. Typically, 0.9 g of $Zn(CH_3COO)_2{\cdot}2H_2O$ was dissolved in 10 mL of DMF (*N*,*N*-dimethylformamide), and then 1.0 g of PAN (polyacrylonitrile, M_w about 150 000) were added and stirred to form a mixed solution. And then 0.33 g commercial Si NPs was added in the above solution. After vigorous stirring for 50 h at 60 °C, a sticky sol was obtained. A high voltage power supply was used to provide a 18 kV high voltage for the as-prepared electrospinning solutions. The feed speed rate and the needle-to-collector distance were set up at 0.8 mL h^{-1} and 15 cm, respectively. The nanofibers were collected on a self-manufactured collector, and then dried for 24 h under vacuum at 80 °C. The dried nanofibers were further stabilized in air at 260 °C for 3 h with a heating rate of 2 °C min^{-1}. Finally, the stabilized nanofibers were annealed in an Ar flow at 900 °C for 1 h with a heating rate of 2 °C min^{-1} for forming ZnO-Si@C-PCNF composites. Furthermore, the Ag nanoparticles modified ZnO-Si@C-PCNFs were prepared via dipping and annealing methods. 100 mg ZnO-Si@C-PCNF composites were added in 20 mL in DI·H_2O/C_2H_5OH mixed solutions containing 9.0 mg $AgNO_3$ under vigorous stirring at 50 °C to evaporate solvents. And then the obtained products were annealed in an Ar flow at 500 °C for 0.5 h with a heating rate of 2 °C min^{-1} for forming Ag/ZnO-Si@C-PCNF composites.

The samples were characterized by XRD (RIGAKU SCXmini) using Cu-Kα radiation (λ = 1.54050 Å) within a diffraction angle (2θ) from 10° to 80°, XPS (VG Scientific ESCALAB MK II) executed on an Axis Ultra photo electron spectrometer using an Al K α (1486.7 eV) X-ray source, SEM (JSM-6700F), transmission electron microscope (TEM, FEI Titan G2 60-300 and Philips Tecnai F20), ICP (Horiba Scientific, Jobin Yvon Ultima 2) and thermal gravimetry analyses (TGA, NETZSCH STA449C) recorded on under air flow with a temperature ramp of 10 °C min^{-1}. And the specific surface area and porosity were performed at 77 K on an Autosorb-iQ2-XR (Quantachrome Instruments).

Coin-Type Cells Assembly and Electrochemical Measurements: The electrochemical behaviors were measured via CR2025 coin-type cells assembled in a high purity argon-filled glove box. The testing electrodes were prepared by mixing 80 wt% active material, 10 wt% acetylene black, and 10 wt% polymer binders (carboxymethyl cellulose, Na-CMC) dissolved in deionized water to form a slurry, which was then pasted on current collector. Subsequently, the prepared electrodes were dried in a vacuum oven at 100 °C overnight. The test cells consisted of working electrode (1.3 ± 0.2 mg cm^{-2}) and lithium sheet which were separated by porous polypropylene separator (Celgard 2400, Hoechst Celanese) and electrolyte of 1 M $LiPF_6$ in EC:EMC:DMC (1:1:1 in volume). The electrochemical properties were all calculated based on the overall mass of the active material of ZnO-Si@C-PCNFs or Ag/ZnO-Si@C-PCNFs. Galvanostatic discharge and charge experiments of the coin cells were conducted by LAND2001A at room temperature. CV and EIS measurements were performed on a CHI760E Electrochemical Workstation with a voltage range from 0.01 to 3.0 V at different scan rates and in the frequency range of 1 mHz–100 kHz at an AC voltage of 5 mV referring to open circuit potential, respectively.

Simple Pouch Full Cells Assembly and Electrochemical Measurements: Here, cathode material of commercial $LiNi_{0.5}Co_{0.2}Mn_{0.3}O_2$ (NCM523) with reversible capacity of 150 mA h g^{-1} and anode material of

commercial graphite with reversible capacity of 310 mA h g^{-1} were purchased from MTI Corporation (Shenzhen) and used without further treatment. The electrodes of NCM523 and graphite were prepared according on commercial full battery standard as shown in Figure S14 in the Supporting Information. The compared electrodes of Ag/ZnO-Si@C-PCNFs were prepared under the same condition above mentioned in Part 2.2 without roll treatment. For the full-cell assembly, the cathode capacity was limited and the capacity of anode was excess. The typical active material loading of the electrode was 3.1 ± 0.1 mg cm^{-2} with ≈3.5 mA h cm^{-1}, of which reversible capacity was about 1.2 times larger than that of NCM523 electrodes with designed 20.0 mg cm^{-2} loading. The coating electrode was cut into small pieces each with area of 5.0 × 6.0 mm^2. Before assembling full-cell test, the cut Ag/ZnO-Si@C-PCNF electrodes were first prelithiated for 30 min via direct touch with Li foil under the presence of electrolyte. The specific capacity of the full cell was calculated based on the weight of NCM523 cathode. The assembled batteries need to undergo a rigorous activation process. The packed pouch cell was pressed tightly and placed in oven overnight at 45 °C. The pouch cell was first charged at 0.02 C rate (1 C = 150 mA h g^{-1}) for 150 min and further charged at 0.05 C until it reaches 3.96 V, and then charged at constant voltage of 3.96 V until its current reaches 0.02 C at 30 °C for the first cycling process. Subsequently, galvanostatic discharge/charge experiments of the Ag/ZnO-Si@C-PCNFs//NCM523 full cells were conducted between 3.0 and 4.2 V by LAND2001A at room temperature.

Supporting Information

Supporting Information is available from the Wiley Online Library or from the author.

Acknowledgements

This work was jointly supported by the Natural Science Foundation of Fujian Province (Grant No. 2017J01035), the Research Grants Council of Hong Kong (Project No. 9440152 and Project No. 9440170), and the National Natural Science Foundation of China (No. 21203025 and No. 61574037).

Conflict of Interest

The authors declare no conflict of interest.

Keywords

electrochemical mechanism, lithium-ion batteries, silicon/carbon nanofiber anodes, simple pouch full cells

Received: January 24, 2019
Revised: March 14, 2019
Published online:

[1] B. Dunn, H. Kamath, J.-M. Tarascon, *Science* **2011**, *334*, 928.
[2] M. N. Obrovac, V. L. Chevrier, *Chem. Rev.* **2014**, *114*, 11444.
[3] J. W. Choi, D. Aurbach, *Nat. Rev. Mater.* **2016**, *1*, 16013.
[4] A. Franco Gonzalez, N.-H. Yang, R.-S. Liu, *J. Phys. Chem. C* **2017**, *121*, 27775.
[5] S. Guo, H. Li, Y. Li, Y. Han, K. Chen, G. Xu, Y. Zhu, X. Hu, *Adv. Energy Mater.* **2018**, *8*, 1800434.
[6] L. Shi, C. Pang, S. Chen, M. Wang, K. Wang, Z. Tan, P. Gao, J. Ren, Y. Huang, H. Peng, Z. Liu, *Nano Lett.* **2017**, *17*, 3681.
[7] F. Lyu, Z. Sun, B. Nan, S. Yu, L. Cao, M. Yang, M. Li, W. Wang, S. Wu, S. Zeng, H. Liu, Z. Lu, *ACS Appl. Mater. Interfaces* **2017**, *9*, 10699.
[8] X. Zuo, J. Zhu, P. Müller-Buschbaum, Y.-J. Cheng, *Nano Energy* **2017**, *31*, 113.
[9] K. Feng, M. Li, W. Liu, A. G. Kashkooli, X. Xiao, M. Cai, Z. Chen, *Small* **2018**, *14*, 1702737.
[10] S. H. Lee, J. H. Lee, D. H. Nam, M. Cho, J. Kim, C. Chanthad, Y. Lee, *ACS Appl. Mater. Interfaces* **2018**, *10*, 16449.
[11] S. H. Kim, Y. S. Kim, W. J. Baek, S. Heo, D. J. Yun, S. Han, H. Jung, *ACS Appl. Mater. Interfaces* **2018**, *10*, 24549.
[12] M. V. Shelke, H. Gullapalli, K. Kalaga, M.-T. F. Rodrigues, R. R. Devarapalli, R. Vajtai, P. M. Ajayan, *Adv. Mater. Interfaces* **2017**, *4*, 1601043.
[13] M. Yao, Z. Zeng, H. Zhang, J. Yan, X. Liu, *Electrochim. Acta* **2018**, *281*, 312.
[14] T. Ma, X. Yu, H. Li, W. Zhang, X. Cheng, W. Zhu, X. Qiu, *Nano Lett.* **2017**, *17*, 3959.
[15] J. Wang, L. Liao, Y. Li, J. Zhao, F. Shi, K. Yan, A. Pei, G. Chen, G. Li, Z. Lu, Y. Cui, *Nano Lett.* **2018**, *18*, 7060.
[16] N. Liu, L. Hu, M. T. McDowell, A. Jackson, Y. Cui, *ACS Nano* **2011**, *5*, 6487.
[17] F. Zhang, L. Wan, J. Chen, X. Li, X. Yan, *Electrochim. Acta* **2018**, *280*, 86.
[18] Q. Chen, R. Zhu, S. Liu, D. Wu, H. Fu, J. Zhu, H. He, *J. Mater. Chem. A* **2018**, *6*, 6356.
[19] S. Suresh, Z. P. Wu, S. F. Bartolucci, S. Basu, R. Mukherjee, T. Gupta, P. Hundekar, Y. Shi, T. M. Lu, N. Koratkar, *ACS Nano* **2017**, *11*, 5051.
[20] H. Li, X. Huang, L. Chen, G. Zhou, Z. Zhang, D. Yu, Y. Jun Mo, N. Pei, *Solid State Ionics* **2000**, *135*, 181.
[21] X. H. Liu, L. Zhong, S. Huang, S. X. Mao, T. Zhu, J. Y. Huang, *ACS Nano* **2012**, *6*, 1522.
[22] L. Li, Z. Zuo, H. Shang, F. Wang, Y. Li, *Nano Energy* **2018**, *53*, 135.
[23] S. Chen, L. Shen, P. A. van Aken, J. Maier, Y. Yu, *Adv. Mater.* **2017**, *29*, 1605650.
[24] H. Shang, Z. Zuo, L. Yu, F. Wang, F. He, Y. Li, *Adv. Mater.* **2018**, *30*, 1801459.
[25] L. Wang, T. Liu, X. Peng, W. Zeng, Z. Jin, W. Tian, B. Gao, Y. Zhou, P. K. Chu, K. Huo, *Adv. Funct. Mater.* **2018**, *28*, 1704858.
[26] W. Zeng, L. Wang, X. Peng, T. Liu, Y. Jiang, F. Qin, L. Hu, P. K. Chu, K. Huo, Y. Zhou, *Adv. Energy Mater.* **2018**, *8*, 1702314.
[27] G. Zhang, Y. Yang, Y. Chen, J. Huang, T. Zhang, H. Zeng, C. Wang, G. Liu, Y. Deng, *Small* **2018**, *14*, 1801189.
[28] K. Ogata, S. Jeon, D. S. Ko, I. S. Jung, J. H. Kim, K. Ito, Y. Kubo, K. Takei, S. Saito, Y. H. Cho, H. Park, J. Jang, H. G. Kim, J. H. Kim, Y. S. Kim, W. Choi, M. Koh, K. Uosaki, S. G. Doo, Y. Hwang, S. Han, *Nat. Commun.* **2018**, *9*, 479.
[29] G. Wang, Z. Wen, Y.-E. Yang, J. Yin, W. Kong, S. Li, J. Sun, S. Ji, *J. Mater. Chem. A* **2018**, *6*, 7557.
[30] Y. Chen, Y. Hu, Z. Shen, R. Chen, X. He, X. Zhang, Y. Zhang, K. Wu, *Electrochim. Acta* **2016**, *210*, 53.
[31] L. Fei, B. P. Williams, S. H. Yoo, J. Kim, G. Shoorideh, Y. L. Joo, *ACS Appl. Mater. Interfaces* **2016**, *8*, 5243.
[32] Y. Chen, Y. Hu, J. Shao, Z. Shen, R. Chen, X. Zhang, X. He, Y. Song, X. Xing, *J. Power Sources* **2015**, *298*, 130.
[33] B. Zhu, N. Liu, M. McDowell, Y. Jin, Y. Cui, J. Zhu, *Nano Energy* **2015**, *13*, 620.
[34] D. Kim, M. Park, S. M. Kim, H. C. Shim, S. Hyun, S. M. Han, *ACS Nano* **2018**, *12*, 10903.
[35] J. Shin, E. Cho, *Chem. Mater.* **2018**, *30*, 3233.
[36] S. Yin, D. Zhao, Q. Ji, Y. Xia, S. Xia, X. Wang, M. Wang, J. Ban, Y. Zhang, E. Metwalli, X. Wang, Y. Xiao, X. Zuo, S. Xie, K. Fang, S. Liang, L. Zheng, B. Qiu, Z. Yang, Y. Lin, L. Chen, C. Wang, Z. Liu, J. Zhu, P. Muller-Buschbaum, Y. J. Cheng, *ACS Nano* **2018**, *12*, 861.

[37] Y. Xing, T. Shen, T. Guo, X. Wang, X. Xia, C. Gu, J. Tu, *J. Power Sources* **2018**, *384*, 207.
[38] H. Song, S. Wang, X. Song, H. Yang, G. Du, L. Yu, J. Xu, P. He, H. Zhou, K. Chen, *J. Mater. Chem. A* **2018**, *6*, 7877.
[39] J. Su, C. Zhang, X. Chen, S. Liu, T. Huang, A. Yu, *J. Power Sources* **2018**, *381*, 66.
[40] Y. An, H. Fei, G. Zeng, L. Ci, S. Xiong, J. Feng, Y. Qian, *ACS Nano* **2018**, *12*, 4993.
[41] G. H. An, D. Y. Lee, H. J. Ahn, *ACS Appl. Mater. Interfaces* **2017**, *9*, 12478.
[42] X. H. Zhang, D. B. Kong, X. L. Li, L. J. Zhi, *Adv. Funct. Mater.* **2019**, *29*, 1806061.
[43] G. D. Li, L. Q. Xu, Y. J. Zhai, Y. P. Hou, *J. Mater. Chem. A* **2015**, *3*, 14298.
[44] F. Li, Z. Z. Wang, W. Q. Liu, T. Yan, C. X. Zhai, P. Wu, Y. M. Zhou, *ACS Appl. Energy Mater.* **2019**, *2*, 2268.
[45] Q. B. Zhang, H. X. Chen, L. L. Luo, B. Zhao, H. Luo, X. Han, J. W. Wang, C. M. Wang, Y. Yang, T. Zhu, M. L. Liu, *Energy Environ. Sci.* **2018**, *11*, 669.
[46] G. F. Ortiz, Á. Berenguer-Murcia, M. Cabello, D. Cazorla-Amorós, J. L. Tirado, *Electrochim. Acta* **2015**, *166*, 293.
[47] H. J. Kim, S. Choi, S. J. Lee, M. W. Seo, J. G. Lee, E. Deniz, Y. J. Lee, E. K. Kim, J. W. Choi, *Nano Lett.* **2016**, *16*, 282.
[48] Y. Shi, M. Zhang, C. Fang, Y. S. Meng, *J. Power Sources* **2018**, *394*, 114.
[49] P. Nie, Z. Le, G. Chen, D. Liu, X. Liu, H. B. Wu, P. Xu, X. Li, F. Liu, L. Chang, X. Zhang, Y. Lu, *Small* **2018**, *14*, 1800635.
[50] J. M. Kim, V. Guccini, K.-d. Seong, J. Oh, G. Salazar-Alvarez, Y. Piao, *Carbon* **2017**, *118*, 8.
[51] C. Shen, X. Fang, M. Ge, A. Zhang, Y. Liu, Y. Ma, M. Mecklenburg, X. Nie, C. Zhou, *ACS Nano* **2018**, *12*, 6280.
[52] S. Chen, Z. Chen, X. Xu, C. Cao, M. Xia, Y. Luo, *Small* **2018**, *14*, 1703361.